

PAPER

High-dynamic-range 3D shape measurement based on time domain superposition

To cite this article: Liang Zhang *et al* 2019 *Meas. Sci. Technol.* **30** 065004

View the [article online](#) for updates and enhancements.

High-dynamic-range 3D shape measurement based on time domain superposition

Liang Zhang^{1,2}, Qian Chen^{1,2}, Chao Zuo^{1,2}, Tianyang Tao^{1,2}, Yuzhen Zhang¹ and Shijie Feng^{1,2,3} 

¹ Jiangsu Key Laboratory of Spectral Imaging & Intelligent Sense, Nanjing University of Science and Technology, Nanjing, Jiangsu Province 210094, People's Republic of China

² Smart Computational Imaging (SCI) Laboratory, Nanjing University of Science and Technology, Nanjing, Jiangsu Province 210094, People's Republic of China

E-mail: zuochao@njust.edu.cn, ShijieFeng@njust.edu.cn and chenqian@njust.edu.cn

Received 6 November 2018, revised 22 February 2019

Accepted for publication 6 March 2019

Published 30 April 2019



Abstract

Fringe projection is a widely used approach for 3D shape measurements. However, it is ineffective for scenarios with a wide range of reflectivity. In this paper, we propose a technique that can measure high-dynamic-range surfaces without changing camera exposure or projected light intensity. With the strategy of time domain superposition, we can use noisy fringe images to recover phase and geometric shapes accurately for low-reflection and high-reflection regions. The measurement accuracy of low-reflection regions obtained by the proposed method is about three times higher than that of the traditional phase-shifting method. Both simulations and experiments are performed to verify the proposed method.

Keywords: fringe projection profilometry, phase-shifting algorithm, high dynamic range, 3D reconstruction, time domain superposition

(Some figures may appear in colour only in the online journal)

1. Introduction

Fringe projection profilometry (FPP) is one of the most promising 3D measurement techniques [1–3] for its low cost, high accuracy, and fast speed. Normally, a typical FPP system is composed of one camera, one projector, and a processing unit. Generally, revealing detail in the dark area requires high exposures, while preserving detail in the bright area requires low exposures. For most cameras, it is difficult to guarantee the image quality of high-dynamic-range (HDR) objects within a single exposure. To solve this problem, several techniques have been proposed in recent years. These techniques can be classified into two categories: equipment-based techniques and algorithm-based techniques [4].

Equipment-based techniques aim to capture optimal fringe images by tuning the hardware parameters. Zhang *et al* [5] proposed a multi-exposure technique to fuse HDR images by selecting the brightest but not saturated pixels. Similarly, Waddington *et al* [6] presented a method by adaptively adjusting projected light intensities instead of camera

exposure. Lin *et al* [7] proposed an adaptive fringe pattern projection method that can improve measurement efficiency. But it also needs several uniform intensities to calculate the optimal intensity. Given the above, though the equipment-based techniques work well, they require to change the hardware parameters during measurement which tends to reduce the level of measurement automation.

Algorithm-based techniques aim to calculate the real phase from saturated fringe images by specific algorithms. Hu *et al* [8] found that if the phase shift is high enough to obtain at least three unsaturated fringe intensities, the image saturation can be overcome. Similarly, Jiang *et al* [9] used additional inverted fringe patterns to replace the corresponding saturated fringe patterns. Further, Chen *et al* [10] found that the saturated fringe images can be directly used to recover accurate phase when the phase shifting step is large enough. Compared with the equipment-based techniques, the algorithm-based techniques need less manual work. They are especially useful when the adjustment of camera exposure is not allowed. However due to camera exposure dose not change during measurement, two cases may occur: (1) long time exposure

³ Author to whom any correspondence should be addressed.

resulted in saturation of high-reflection regions; (2) short time exposure resulted in low signal-noise-ratio (SNR) of low-reflection regions. We notice that most algorithm-based techniques mainly focus on the first case. While the analysis of the second case is still lacking. In this paper, we aim to extend dynamic range by reducing the phase error of the low-reflection regions. Based on the Gaussian noise model, we proposed an effective algorithm-based method called time domain superposition. The proposed method does not need complex calculation while can maintain high accuracy for HDR objects. Both simulation and experimental results will be presented to validate the proposed method.

The organization of this paper is as follows. Section 2 explains the principle of the proposed method. Section 3 shows the simulation results. Section 4 gives the experimental results. Section 5 discusses additional considerations. Finally, section 6 summarizes the paper.

2. Principle

Different from conventional HDR methods, our focus is on reducing the phase error of the low-reflection regions. For HDR scenes, we first adjust the camera exposure so that the region with the highest reflectivity is not saturated. While the phase accuracy of the low-reflection regions is seriously disturbed by random noise due to insufficient camera exposure. In order to solve this problem, we analyze the noise model of FPP systems and propose an effective method called time domain superposition.

2.1. Noise model of FPP systems

In FPP systems, the projected fringe patterns can be represented as

$$I_k^P = A + B \cdot \cos[\phi - \frac{2k\pi}{N}], \quad (1)$$

where A is the average intensity, B is the intensity modulation, N is the phase-shifting step, k is the phase-shift index ($k = 0, 1, 2, \dots, N-1$), and ϕ is the phase to be measured. Because of the random noise, the captured images I_k^C can be represented as

$$I_k^C = \rho t r I_k^P + I^N, \quad (2)$$

where ρ is the camera sensitivity, t is the exposure time, r is the surface reflectivity, and I^N is the random noise. Then equation (2) can be rewritten as

$$I_k^C = A' + B' \cdot \cos(\phi - \frac{2k\pi}{N}), \quad (3)$$

where

$$A' = \rho t r A + I^N, \quad (4)$$

$$B' = \rho t r B. \quad (5)$$

According to the N -step phase-shifting algorithm, ϕ can be extracted by the following equation [11]:

$$\phi = \tan^{-1} \left[\frac{\sum_{k=0}^{N-1} I_k^C \sin(2k\pi/N)}{\sum_{k=0}^{N-1} I_k^C \cos(2k\pi/N)} \right]. \quad (6)$$

Normally, in FPP systems, the random noise is assumed to be additive white Gaussian noise [12]. This assumption is valid for many applications in which thermal or shot noise is the main noise. Moreover, according to the central limit theorem, when independent random noises are added, their properly normalized sum tends toward Gaussian distribution. So without knowing the real noise distribution, the Gaussian noise model is valid for FPP systems in actual measurement. With the mathematic derivation [13], we can estimate the change of ϕ with respect to A' , as shown in equation (7):

$$\Delta\phi = \frac{2}{NB'} \left[\sum_{k=0}^{N-1} \sin(\phi + 2k\pi/N) \right] \Delta A'. \quad (7)$$

Since the random noise has zero mean [14], the variance of phase error σ_ϕ^2 can be represented as

$$\sigma_\phi^2 = \left(\frac{2\sigma}{NB'} \right)^2 \sum_{k=0}^{N-1} \sin^2(\phi + 2k\pi/N) = \frac{2\sigma^2}{NB'^2} = \frac{2\sigma^2}{N\rho^2 t^2 r^2 B^2} \quad (8)$$

where σ_ϕ is the standard deviation of phase error, and σ is the standard deviation of the random noise. From equation (8), we can see that once the phase-shifting step N , the intensity modulation B , and camera parameters are predetermined, σ_ϕ^2 only depends on the surface reflectivity r and the random noise variance σ^2 . Since r cannot be changed artificially, one can reduce the phase error by decreasing σ^2 .

2.2. Time domain superposition

From the previous section, we know that the measurements are modeled as the true values plus independent Gaussian errors. So we can use Gaussian denoising algorithms to decrease the influence of noise. In this paper, we propose a method called time domain superposition to reduce the random noise by superimposing a set of replicate measurements. Mathematically, the time domain superposition method can be described as

$$I' = \sum_{i=1}^n (I_{ki}^C), \quad (9)$$

$$\phi = \tan^{-1} \left\{ \frac{\sum_{k=0}^{N-1} [I' \cdot \sin(2k\pi/N)]}{\sum_{k=0}^{N-1} [I' \cdot \cos(2k\pi/N)]} \right\} \quad (10)$$

where n is the superposition times, I_{ki}^C is the I_k^C of i th measurement, and I' is the sum of all the I_{ki}^C . Assuming the expected value of I_{ki}^C is μ_1 and the standard deviation of random noise is σ_1 , the SNR of every single measurement can be calculated as [15, 16]

$$\text{SNR}_{\text{single}} = \frac{\mu_1}{\sigma_1}. \quad (11)$$

After time domain superposition, the expected value of I' is

$$\mu_n = \sqrt{E[(I')^2]} = \sqrt{E[(n\mu_1)^2]} = n\mu_1 \quad (12)$$

where $E()$ is the mathematical expectation function. Since the noise variance is constant, its standard deviation after n times superposition is

$$\sigma_n = \sqrt{n(\sigma_1)^2} = \sqrt{n}\sigma_1. \quad (13)$$

According to equations (12) and (13), the SNR of I' can be calculated as

$$\text{SNR}_n = \frac{\mu_n}{\sigma_n} = \sqrt{n} \cdot \text{SNR}_{\text{single}}. \quad (14)$$

It can be seen from equation (14) that the time domain superposition method can improve the SNR of the low-reflection regions by increasing the number of superposition times, thus extending the measurement dynamic range.

3. Simulation

We first simulated the effect of random noise on the high-reflection regions. Assuming the camera is an 8-bit camera, the three-step phase shifting equations can be described as

$$I_k^C = 125 + 125 \cos(\phi - \frac{2k\pi}{3}) \quad k = 1, 2, 3. \quad (15)$$

Figure 1 shows one of the original three phase-shifted fringe patterns. Based on the previous noise model, we added a Gaussian noise with a mean value of zero and a variance of five to the fringe image shown in figure 1(b). Figure 1(f) demonstrates that for the high-reflection regions, the phase error caused by Gaussian noise is quite small, approximately phase root-mean-square error (RMSE) 0.033 rad. And the impact of the Gaussian noise can be negligible after ten times superposition shown in figure 3(a).

Then we simulated the effect of Gaussian noise on the low-reflection regions by decreasing the value of A and B . Equation (15) can be rewritten as:

$$I_k^C = 10 + 10 \cos(\phi - \frac{2k\pi}{3}) \quad k = 1, 2, 3. \quad (16)$$

In such a case, Gaussian noise makes a large impact on the image quality and phase calculation respectively shown in figures 2(d) and (f). However, we can still use the time domain superposition method to get a satisfied phase RMSE at the cost of increasing the number of superposition times shown in figure 3(b).

Overall, time domain superposition can reduce the phase error caused by Gaussian noise effectively for both high-reflection and low-reflection regions.

4. Experimental results

We developed a fringe projection system to evaluate the proposed method. The experimental system includes a digital-light-processing (DLP) projector (model: TI LightCrafter 4500) with a resolution of 912×1140 and a 8-bit digital CMOS

camera (model: *Basler acA640 – 750um*) with a resolution of 640×480 . The camera is attached with a 8mm focal length lens (model: *Computar M0814 – MP2*). In this paper, we used the three-step phase-shifting fringe patterns combined with time domain superposition to obtain the wrapped phase, and the multi-frequency temporal phase unwrapping algorithm [17] to obtain continuous absolute phase. Then we adopted the method of Liu *et al* [18] to map absolute phase to real-world 3D coordinates.

For our projector, the light-emitting diode (LED) current settings control the individual currents of the red, green, and blue LEDs. A setting of 255 corresponds to the maximum LED current. A setting of 0 corresponds to minimum LED current. In the experiments, the blue LED is used to project the fringe patterns because the linear relation between its current value and its brightness is the best. Moreover, the LED current value is used to represent the projected light intensity.

4.1. Precision analysis

We first measured a pair of standard ceramic spheres shown in figure 4(a). The standard ceramic spheres have the diameter of 50.8mm within micron-sized manufacturing error.

To prove that our method can work well for the low-reflection regions, we used a low projected light intensity to take the fringe images shown in figure 5. In this case, the fringe image has limited visibility and poor contrast. Directly using these low SNR fringe images, we got a very poor 3D measurement result shown in figure 6(a). After 30 times superposition, the quality of measurement is improved greatly shown in figure 6(b).

To evaluate our method quantitatively, we used the depth information to perform the spherical fitting, and the fitted spheres were set as the ground truth. Then we used the ground truth to calculate the RMSE of the standard spheres. The experimental result is shown in figure 7. One may notice that when n reaches a certain value, the RMSE becomes a steadily numerical value without large decrease. That's because, for a given photographing environment, the denoising capability of the time domain superposition method is limited by the raw image quality. In other words, we cannot decrease the RMSE infinitely by increasing the superposition times.

In addition, a plane measurement is performed with a white ceramic plate and a black lifting table shown in figure 4(b). In this experiment, the time domain superposition method was compared with two commonly used HDR methods: the multi-exposure method [5] and the inverted-pattern method [9].

Figure 8(a) shows that when the image quality of white plane is good, the black plane has a poor SNR. Figure 8(b) shows that when the black plane has good fringes, the white plane is saturated. For multi-exposure method, at least two exposures are required to measure such a composite scene. After many experiments, we found that the optimal light intensity for white plane is 120 when the camera exposure is 43 000 μs . Moreover, the optimal light intensity for black plane is 120 when the camera exposure is 163 000 μs . Figure 8(c) shows the fusion fringe image. With fusion fringe images, we

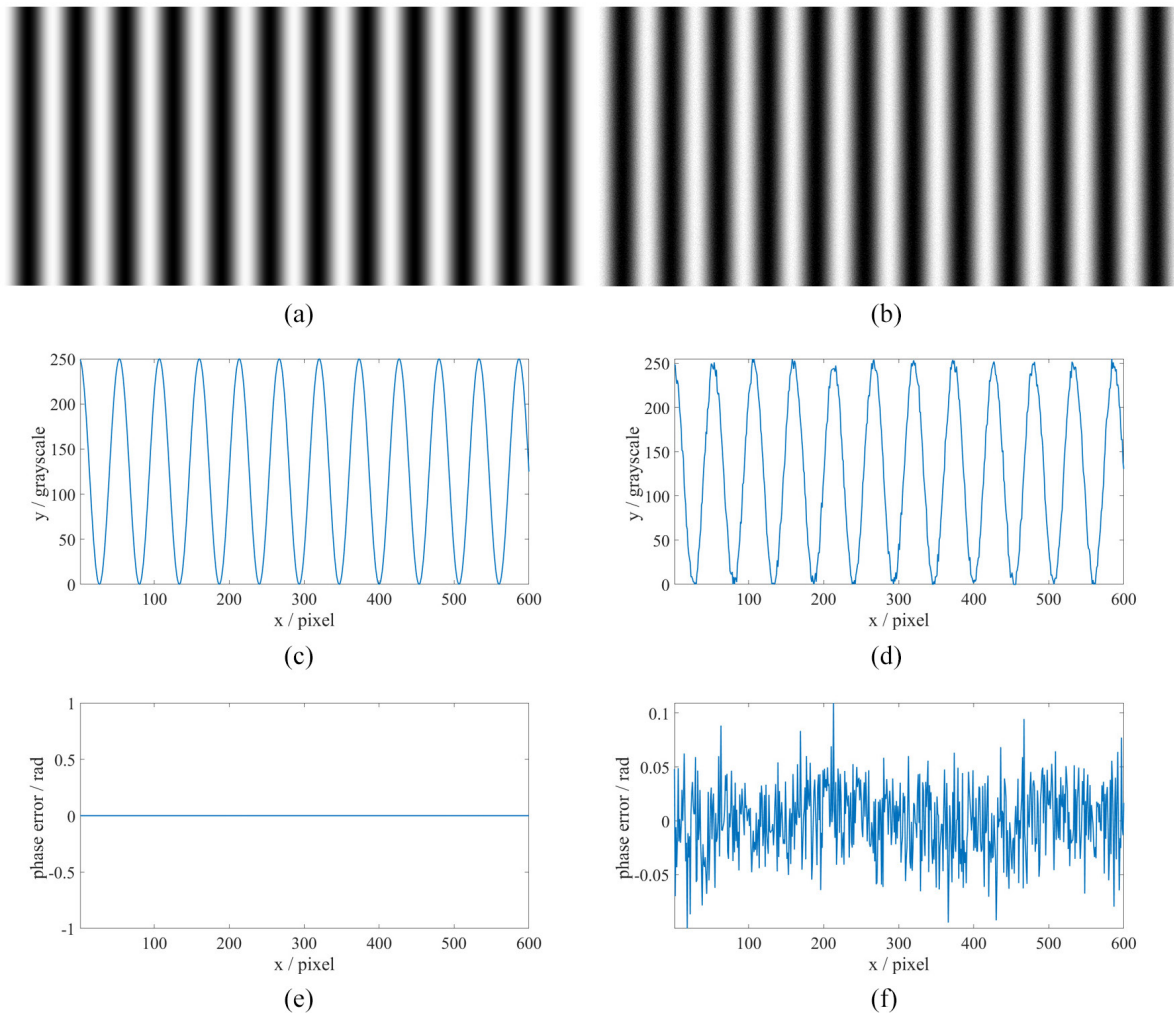


Figure 1. High-reflection regions: (a) one of the noise-free fringe patterns; (b) one of the fringe patterns with the Gaussian noise; (c) cross-section plot of (a); (d) cross-section plot of (b); (e) phase error of (c); (f) phase error of (d).

got high-precision measurement results for both the white and the black planes shown in figures 8(f) and (i).

For inverted-pattern method, it cannot improve the SNR of low-reflection regions shown in figures 9(d) and (g), so its dynamic range depends on the improvement on saturation region. To determine its upper limit value of light intensity, we preliminarily used fringe patterns with the light intensity of 150 to measure the composite scene. The measurement results are shown in figures 9(f) and (i). It can be seen that the measurement of white plane with the light intensity of 150 is worse than that with the light intensity of 50. This means inverted-pattern method is applicable only in limited range. Further experiments suggest the upper limit of its light intensity is 140. Once the upper limit value is exceeded, the phase error of white plane increases along with the increase of light intensity shown in figure 10.

For time domain superposition method, we first adjusted the light intensity to 120 to avoid saturation. After 25 times superposition, the measurement accuracy is increased shown in figures 11(f) and (i). Then we adjusted the light intensity to 50, and we could also get satisfying measurement results shown in figures 11(e) and (h). Further, we adjusted the light

intensity to 15. Figure 11(d) demonstrates that even for such a case, the measurement error of the white plane is still quite small. While the measurement result of the black plane is very poor shown in figure 11(g). That is because, for the extreme low-reflection regions (light intensity is less than 5), the assumption of Gaussian noise is not valid.

The experimental data are listed in table 1, where ‘ET’ means the exposure time, ‘LI’ means the light intensity, ‘n’ is the superposition times, ‘RMSEW’ is the RMSE of the white ceramic plate, and ‘RMSEB’ is the RMSE of the black lifting table. Due to multi-exposure can arbitrarily change the camera exposure, its dynamic range only depends on the hardware parameters of FPP systems. However, the selection of the exposure time is empirical and normally many exposure times are required to realize the HDR measurements which makes the measurement very time-consuming. For the other two methods, we took the RMSEW as the standard to calculate the dynamic range. An acceptable RMSEW should be less than 0.200 mm. In order to meet the above requirement, the realizable light intensity adjustment range of the inverted-pattern method is from 70 to 140. So the dynamic range of inverted-pattern method DP_{inv} can be expressed mathematically as

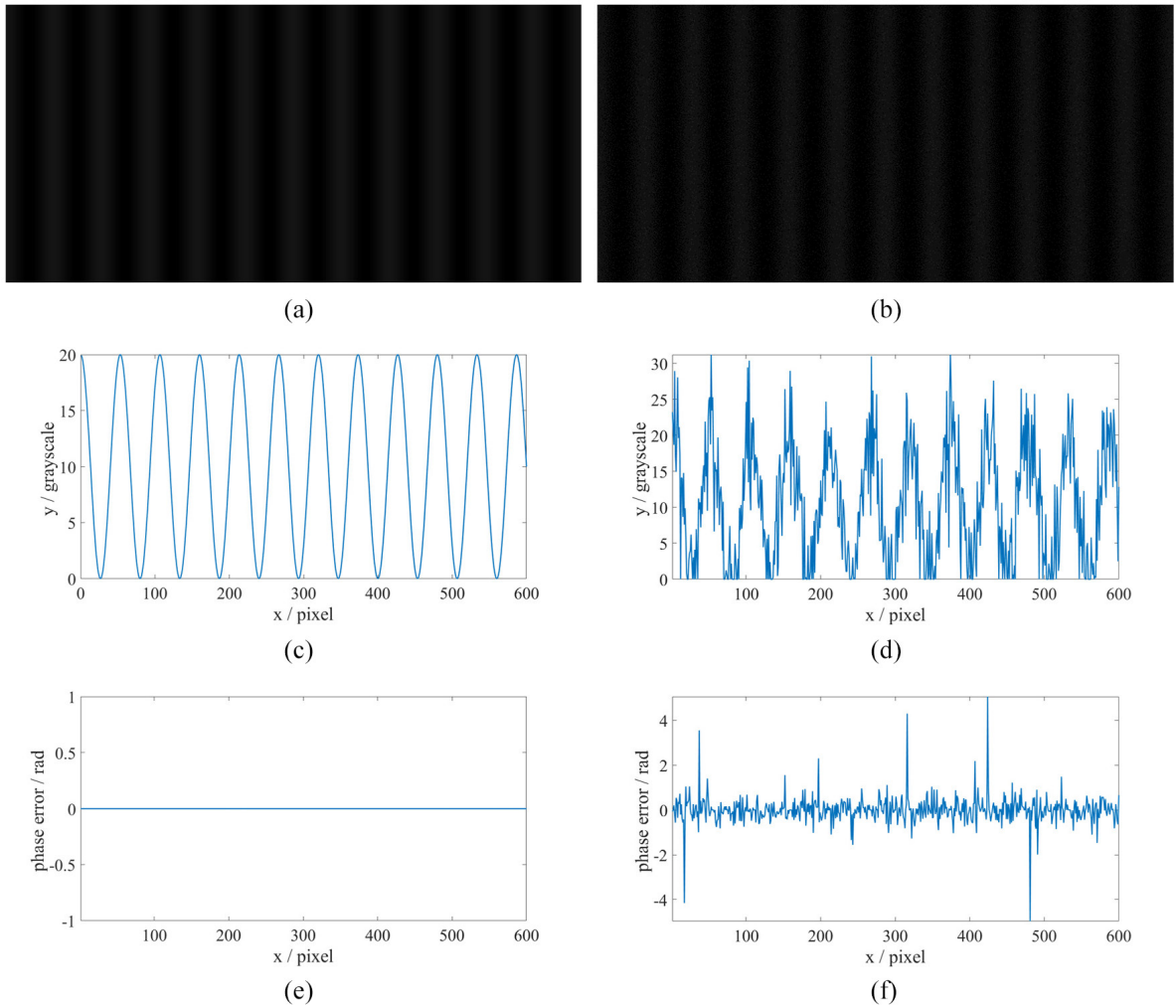


Figure 2. Low-reflection regions: (a) one of the noise-free fringe patterns; (b) one of the fringe patterns with Gaussian noise; (c) cross-section plot of (a); (d) cross-section plot of (b); (e) phase error of (c); (f) phase error of (d).

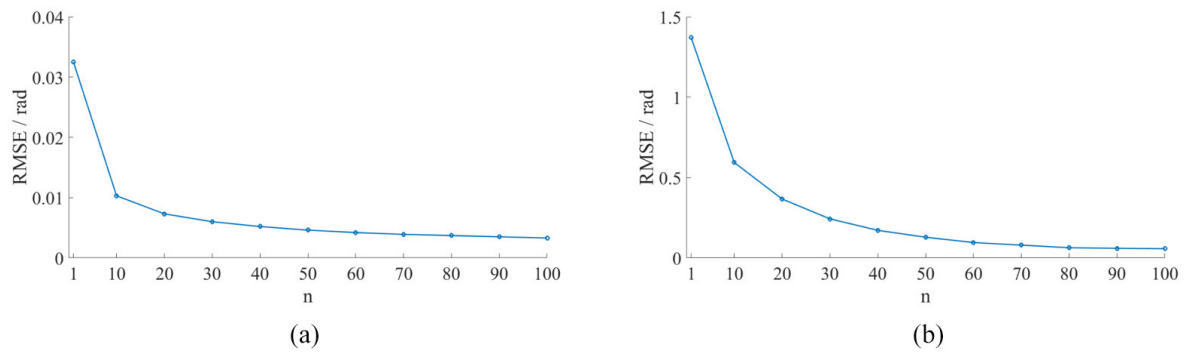


Figure 3. (a) Phase RMSE under the Gaussian noise with different superposition times when intensity modulation is 125; (b) phase RMSE under the Gaussian noise with different superposition times when intensity modulation is 10.

$$DR_{inv} = \frac{140}{70} = 2.0. \quad (17)$$

$$DR_{tim} = \frac{120}{15} = 8.0, \quad (18)$$

Similarly, the dynamic range of the time domain superposition DP_{tim} and that of the normal phase-shifting method DP_{nor} can be calculated as

$$DR_{nor} = \frac{120}{70} \approx 1.7. \quad (19)$$

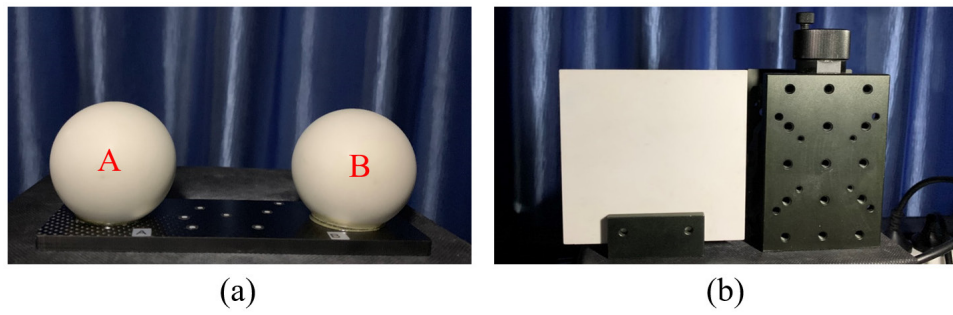


Figure 4. (a) Photograph of the standard ceramic spheres; (b) photograph of the white ceramic plate and black lifting table.

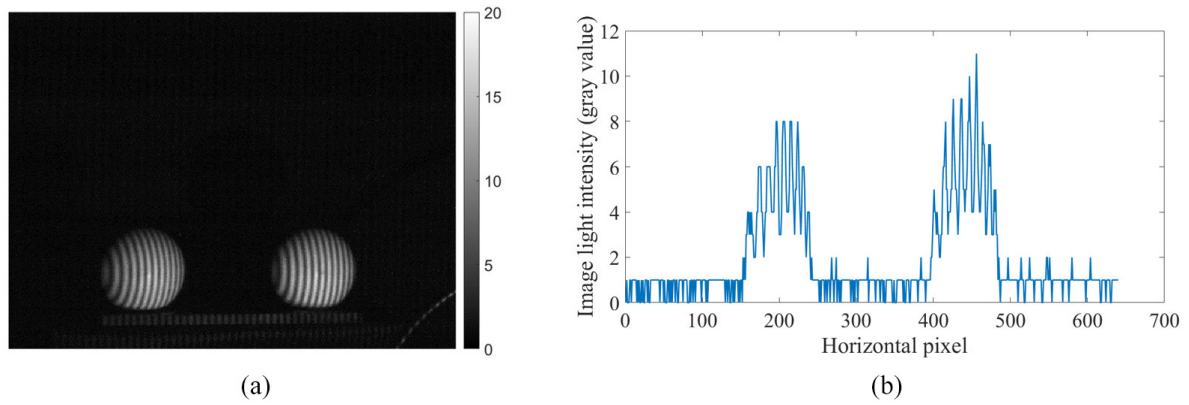


Figure 5. (a) Representative fringe image. (b) Cross-section plot of the 330th row.

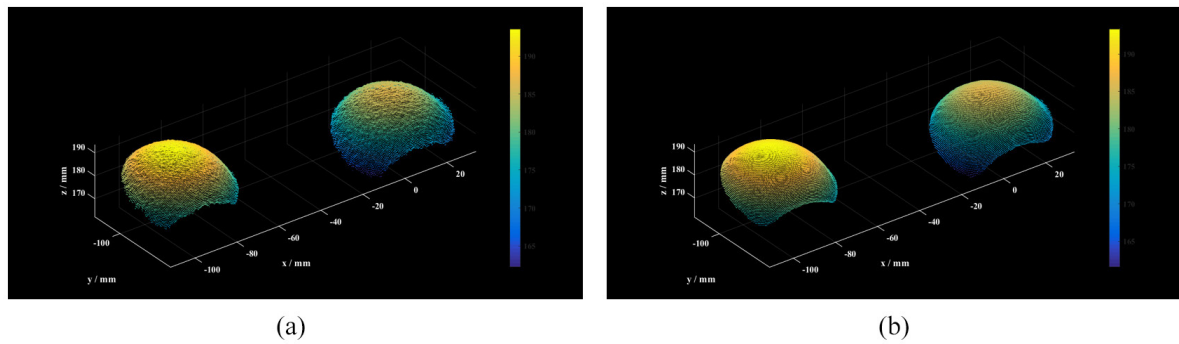


Figure 6. (a) 3D measurement result without superposition. (b) 3D measurement result with 30 times superposition.

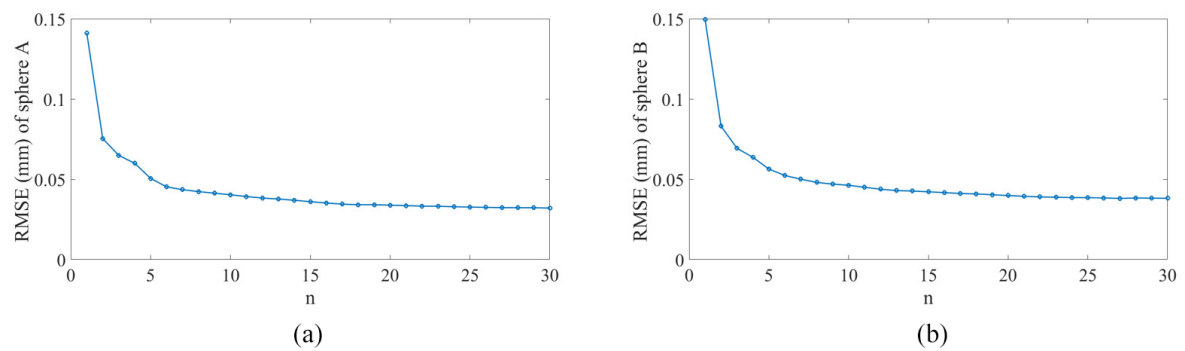


Figure 7. (a) RMSE of the sphere A with different n . (b) RMSE of the sphere B with different n .

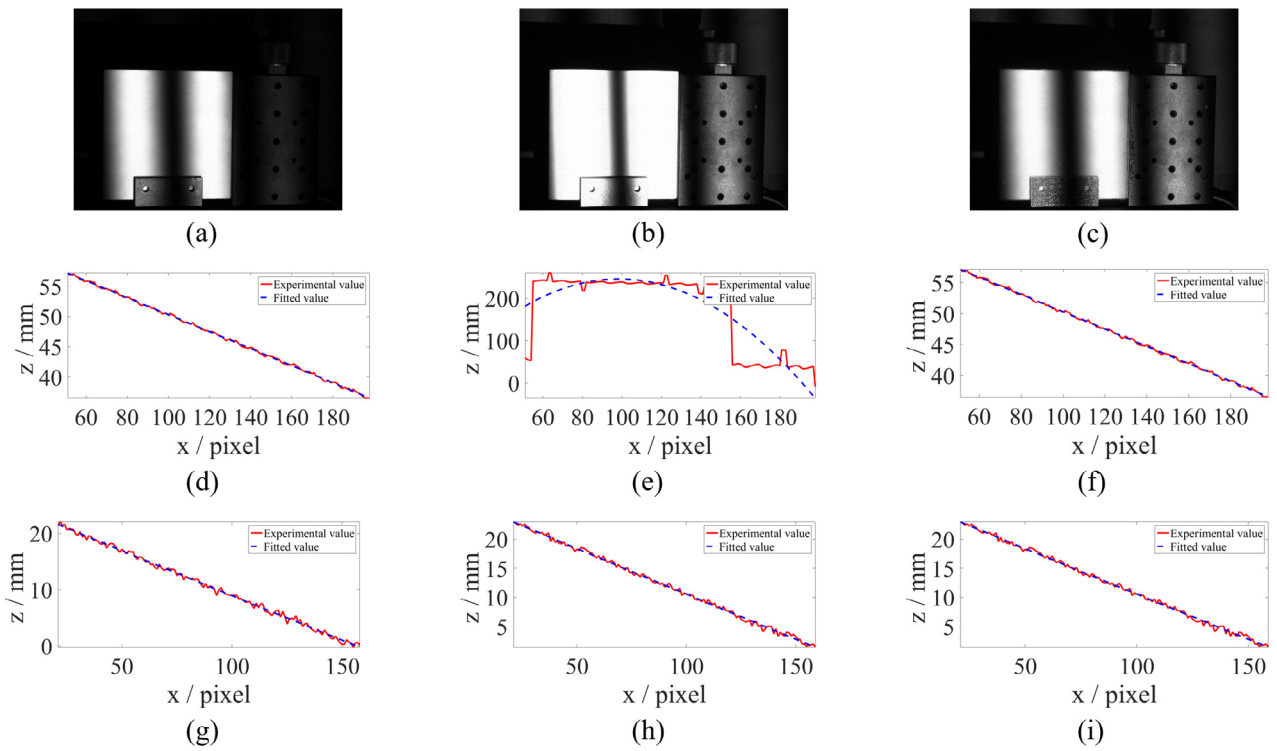


Figure 8. Multi-exposure method: (a) one of the phase-shifting fringe images at exposure time 43 000 μs with light intensity of 120; (b) one of the phase-shifting fringe images at exposure time 163 000 μs with light intensity of 120; (c) one of the fusion fringe images; (d)–(f) cross-section plot of the 3D reconstructions of the white ceramic plate in (a)–(c) respectively; (g)–(i) cross-section plot of the 3D reconstructions of the black lifting table in (a)–(c) respectively.

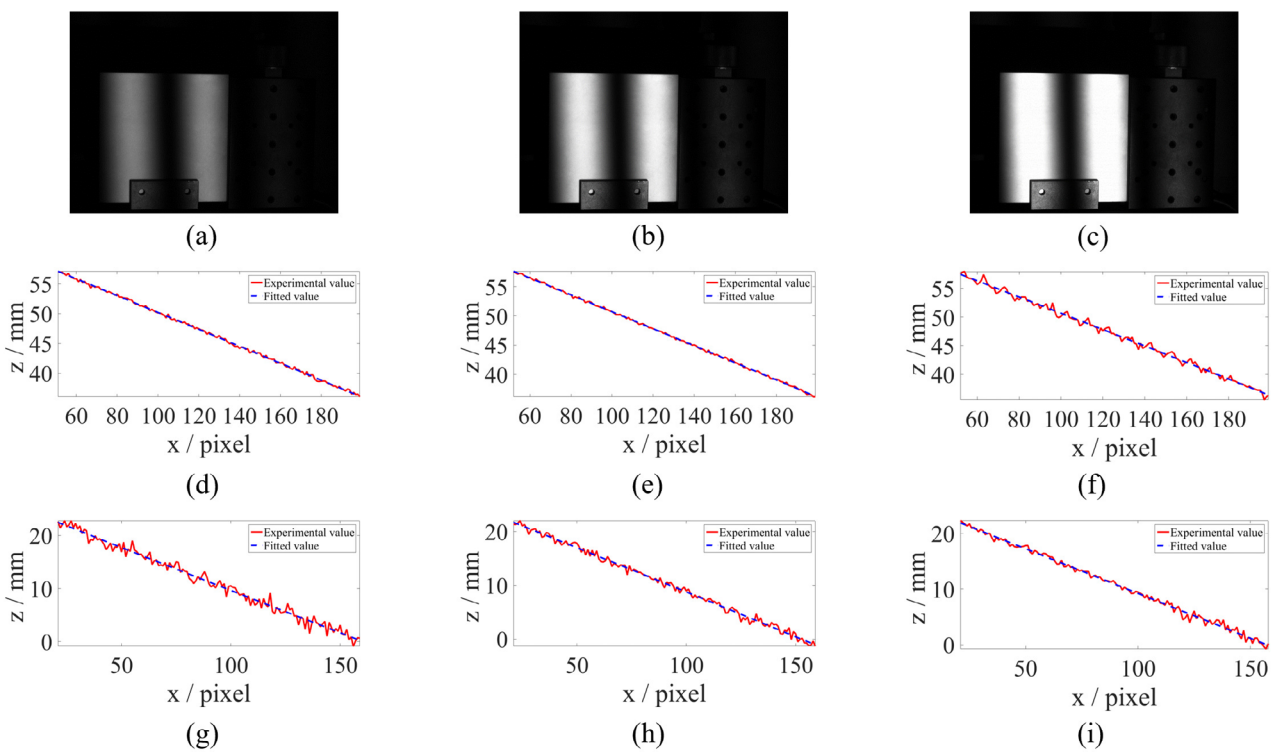


Figure 9. Inverted-pattern method: (a) one of the phase-shifting fringe images at exposure time 43 000 μs with light intensity of 50; (b) one of the phase-shifting fringe images at exposure time 43 000 μs with light intensity of 120; (c) one of the phase-shifting fringe images at exposure time 43 000 μs with light intensity of 150; (d)–(f) cross-section plot of the 3D reconstructions of the white ceramic plate in (a)–(c) respectively; (g)–(i) cross-section plot of the 3D reconstructions of the black lifting table in (a)–(c) respectively.

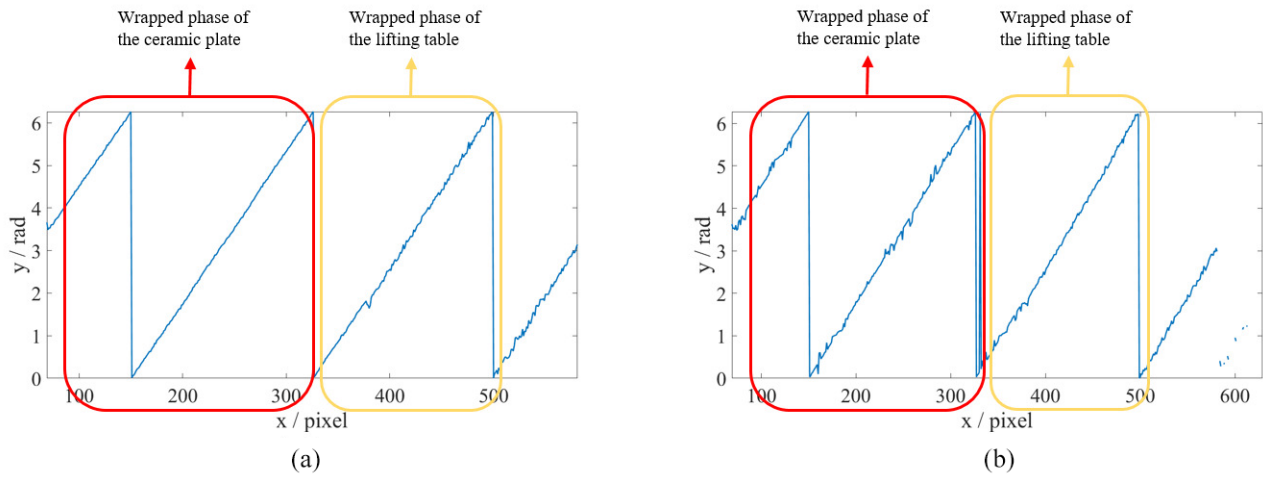


Figure 10. (a) Cross-section plot of the wrapped phase with light intensity of 140; (b) cross-section plot of the wrapped phase with light intensity of 150.

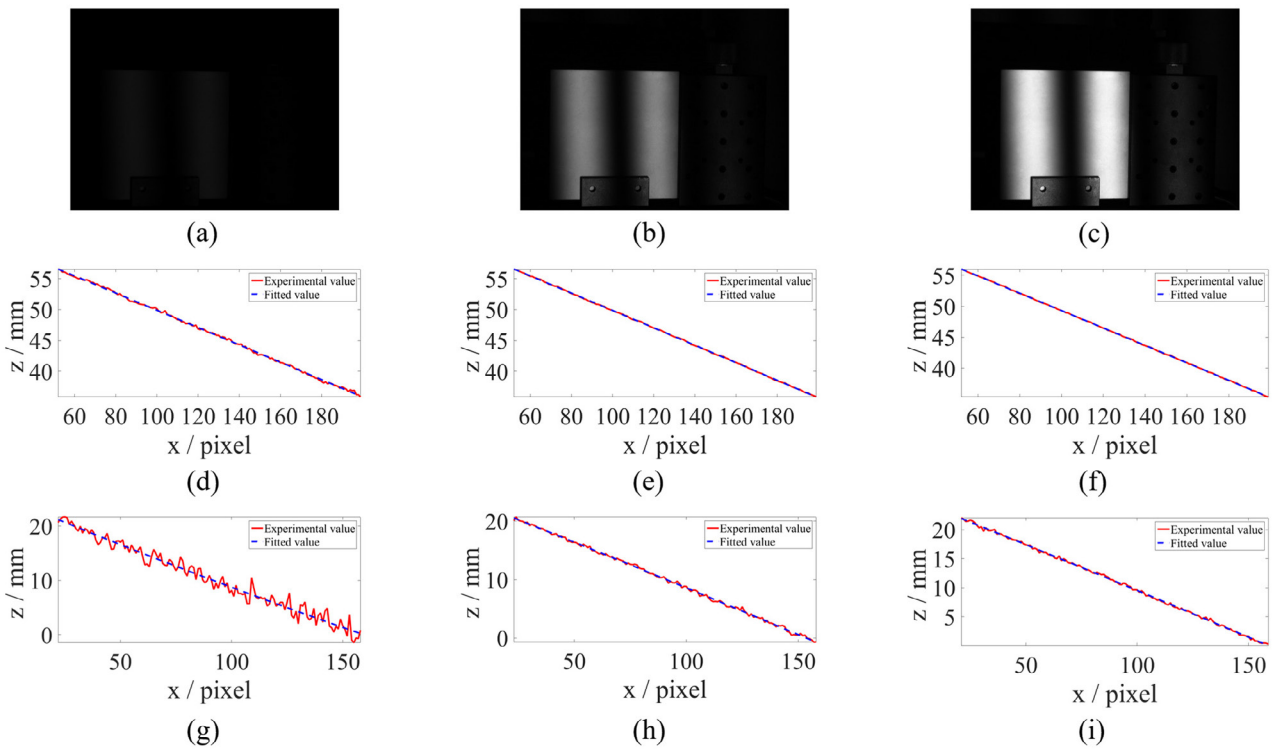


Figure 11. Time domain superposition method: (a) one of the phase-shifting fringe images at exposure time 43 000 μs with light intensity of 15; (b) one of the phase-shifting fringe images at exposure time 43 000 μs with light intensity of 50; (c) one of the phase-shifting fringe images at exposure time 43 000 μs with light intensity of 120; (d)–(f) cross-section plot of the 3D reconstructions of the white ceramic plate in (a)–(c) respectively; (g)–(i) cross-section plot of the 3D reconstructions of the black lifting table in (a)–(c) respectively.

It can be seen that the inverted-pattern method does extend the dynamic range, but not very significantly. By contrast, the dynamic range of our method is about five times larger than that of the normal phase-shifting method. In addition, table 1 shows that the measurement accuracy obtained by our method is about three times higher than those of the other two HDR methods.

4.2. Measurement of complex HDR objects

To further verify the proposed method, we measured two more complex HDR scenes shown in figure 12.

Scene 1 consists of a black plastic block labeled ‘A’, a brown cardboard box labeled ‘B’, a white plaster statue labeled ‘C’, and a blue tape labeled ‘D’ shown in figure 12(a).

Table 1. Experimental data.

Method	ET/ μ s	LI/grayscale	n	RMSEW/mm	RMSEB/mm
Multi-exposure	43 000	120	1	0.178	0.395
	163 000	120	1	43.8	0.199
Phase-reversal	43 000	50	1	0.228	0.829
	43 000	120	1	0.164	0.408
	43 000	150	1	0.425	0.351
Time domain superposition	43 000	15	25	0.193	1.15
	43 000	50	25	0.0652	0.254
	43 000	120	25	0.0477	0.139

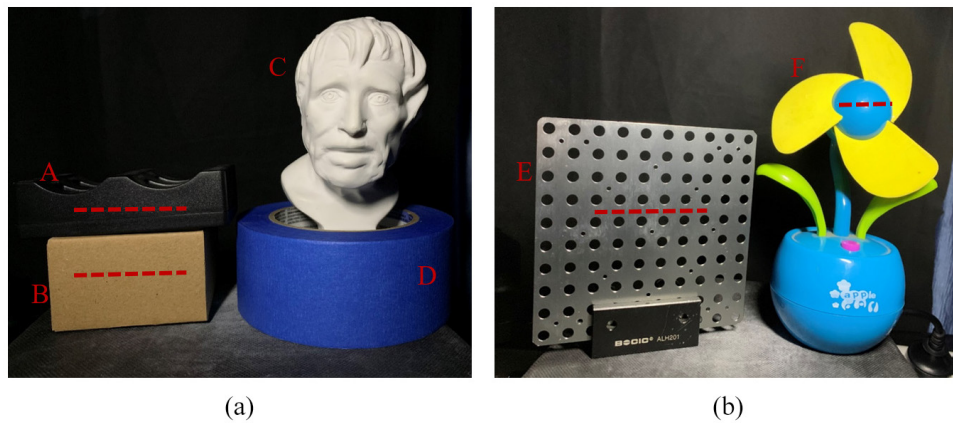


Figure 12. (a) Photograph of the scene 1; (b) photograph of the scene 2.

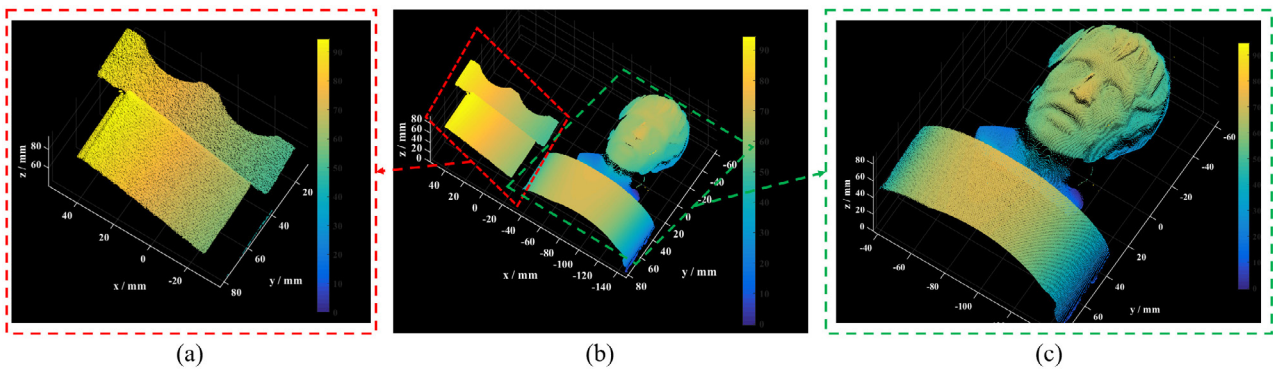


Figure 13. (a) Enlarged detail of the black plastic block and the brown cardboard box; (b) 3D reconstruction of the scene 1; (c) enlarged detail of the white plaster statue and the blue tape.

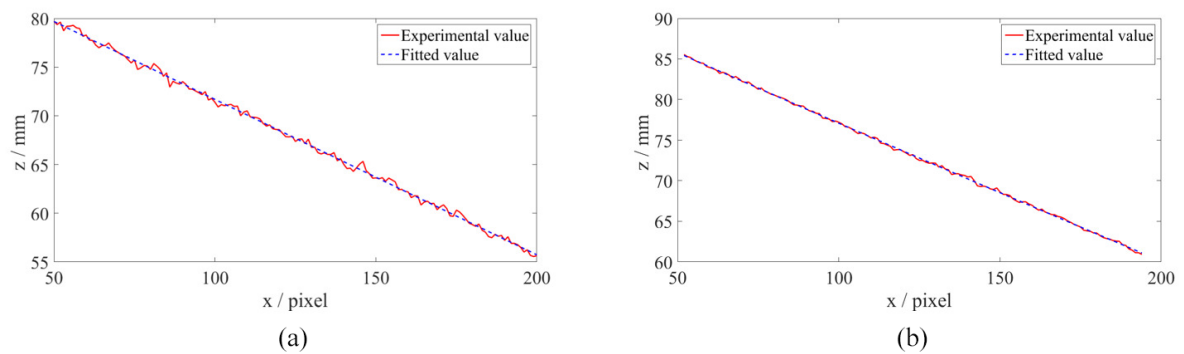


Figure 14. (a) Differences between the ground truth and the measured value of the black plastic block; (b) differences between the ground truth and the measured value of the brown cardboard box.

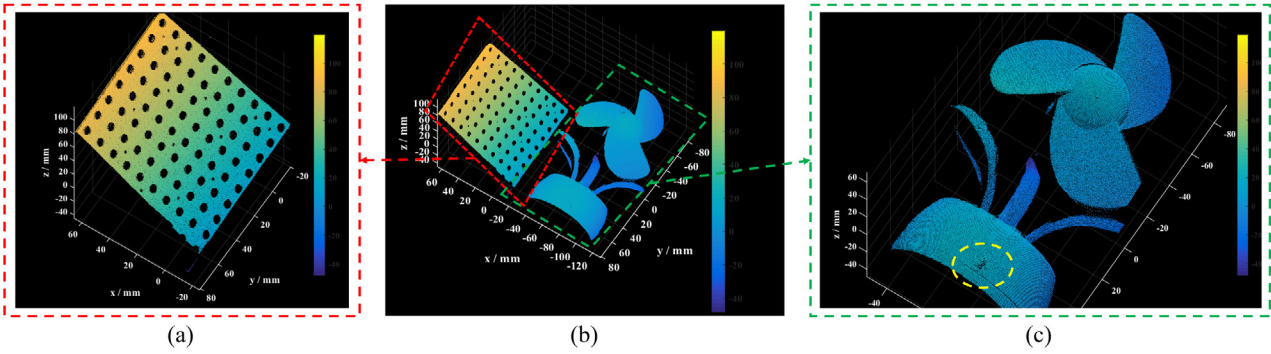


Figure 15. (a) Enlarged detail of the metal plate; (b) 3D reconstruction of the scene 2; (c) enlarged detail of the plastic toy.

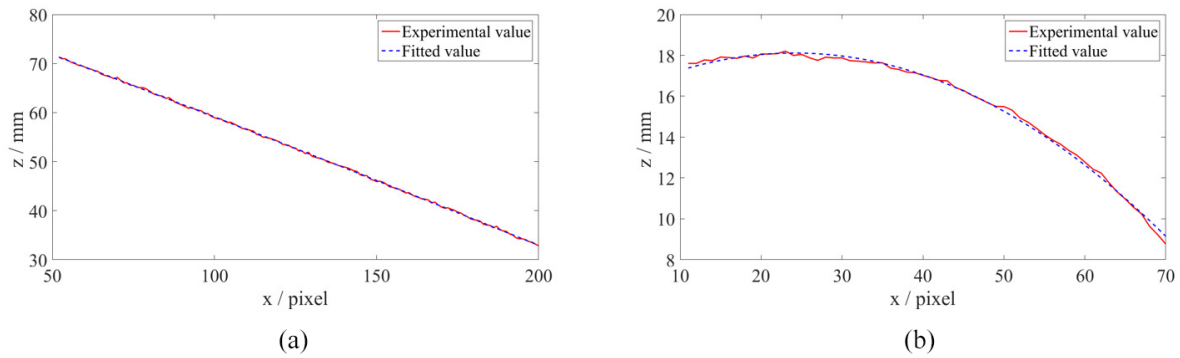


Figure 16. (a) Differences between the ground truth and the measured value of the metal plate; (b) differences between the ground truth and the measured value of the sphere of plastic toy.



Figure 17. (a) Front view of the porcelain bottles; (b) side view of the porcelain bottles.

The 3D reconstruction is shown in figure 13. Here we still set the fitted data as the ground truth. Figure 14 shows the differences between ground truth and measured value of the selected regions marked by dotted red lines in figure 12(a). The RMSE of the black plastic block is 0.207 mm. The RMSE of the brown cardboard box is 0.146 mm. From this experiment, we can see that the proposed method works well for objects with a large variation of reflectivity.

Scene 2 consists of a metal plate labeled ‘E’, and plastic toy labeled ‘F’ shown in figure 12(b). We measured them to verify that the proposed method can be used to measure shiny surfaces. The measurement results are shown in figures 15 and 16. The RMSE of the metal plate is 0.159 mm, and the RMSE of the sphere of plastic toy is 0.146 mm. The obvious

measurement error circled in yellow shown in figure 15(c) is caused by specular reflection. The problem of specular reflection is discussed in the next subsection.

4.3. Measurement of objects with specular reflection

In this experiment, we measured two porcelain bottles shown in figure 17. Because of the material property of porcelain, these two bottles are prone to emerge specular reflection regions on their surface. Different with diffuse reflection, specular reflection can hardly be removed by reducing camera exposure or projected light intensity shown in figure 18. That means techniques based on adjusting the parameters of cameras and projectors cannot measure objects with specular

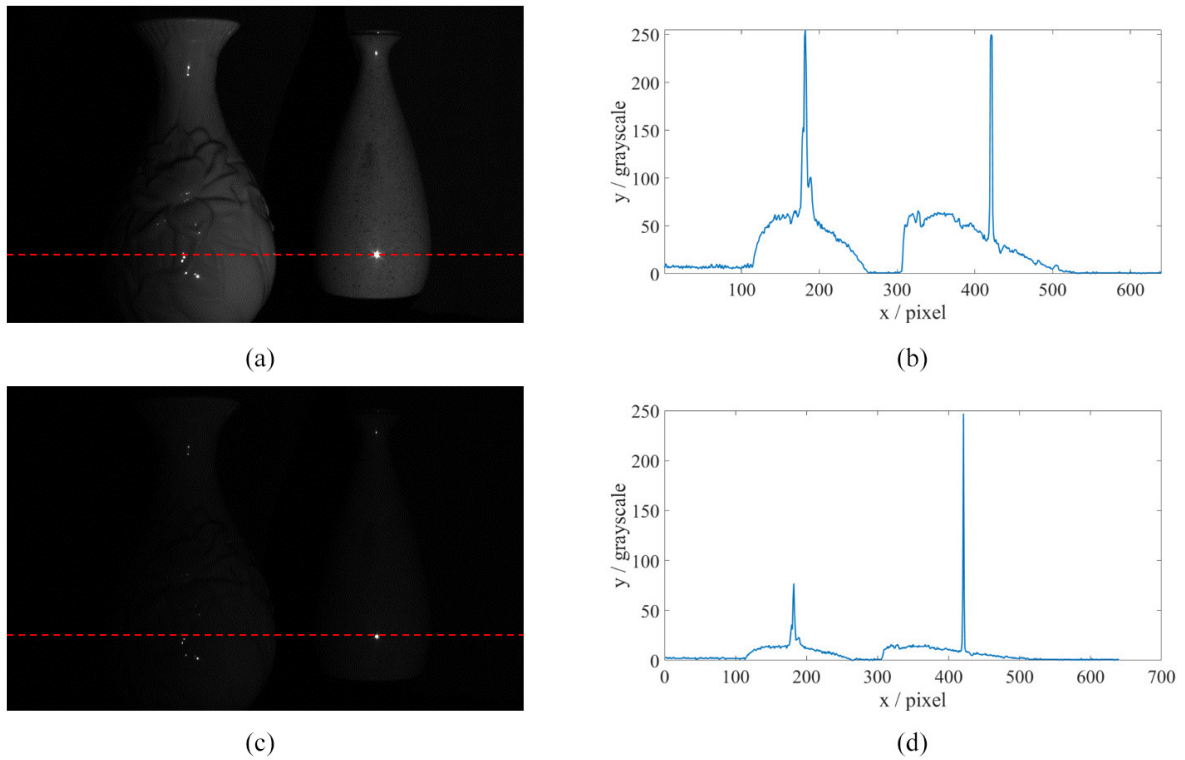


Figure 18. (a) One of the phase-shifting fringe images at exposure time $4300 \mu\text{s}$ with light intensity of 30; (b) cross-section plot of the row marked by dotted red lines in (a); (c) one of the phase-shifting fringe images at exposure time $4300 \mu\text{s}$ with light intensity of 90; (d) cross-section plot of the row marked by dotted red lines in (c).

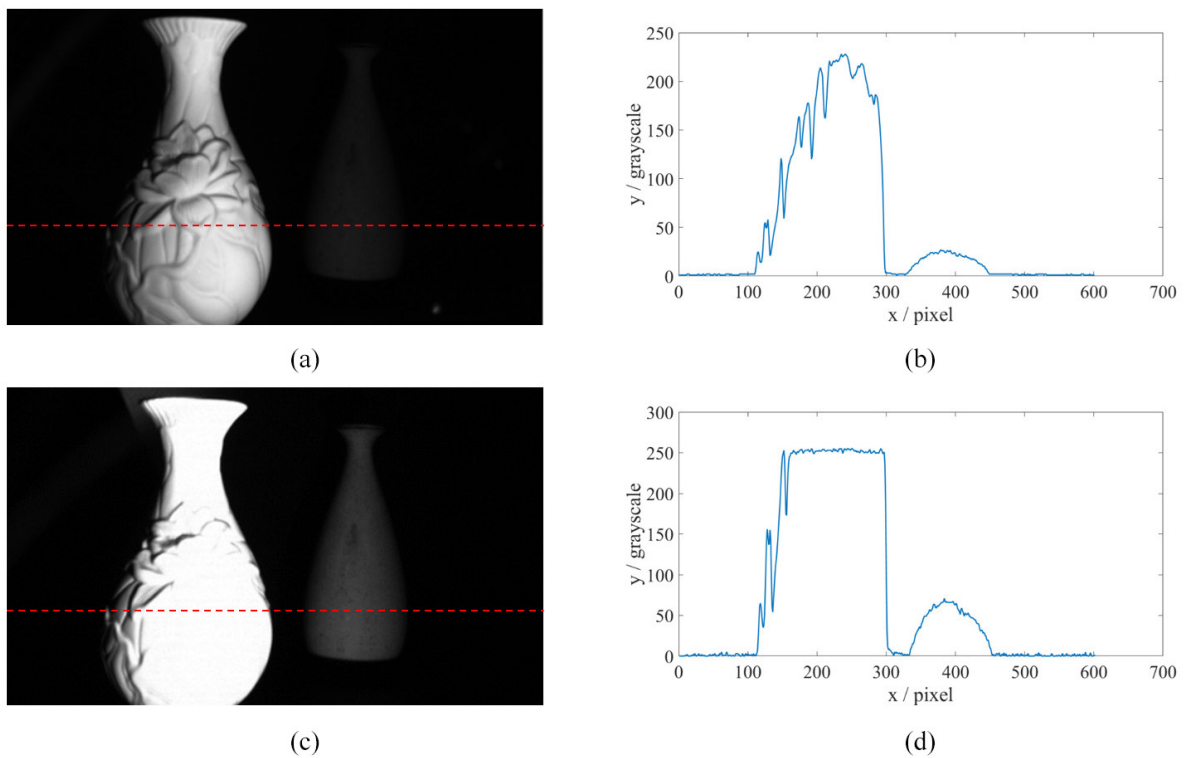


Figure 19. (a) One of the phase-shifting fringe images at exposure time $53000 \mu\text{s}$ after application of polarizer; (b) cross-section plot of the row marked by dotted red lines in (a); (c) one of the phase-shifting fringe images at exposure time $113000 \mu\text{s}$ after application of polarizer; (d) cross-section plot of the row marked by dotted red lines in (c).

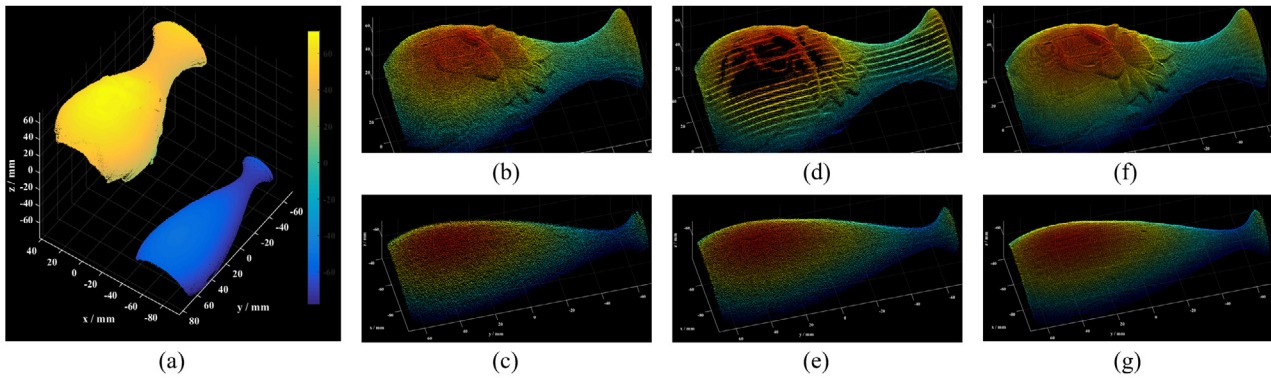


Figure 20. (a) 3D reconstruction of the white and cyan bottles; (b) local enlarged drawing of the white bottles at exposure time 53 000 μs ; (c) local enlarged drawing of the cyan bottles at exposure time 53 000 μs ; (d) local enlarged drawing of the white bottles at exposure time 113 000 μs ; (e) local enlarged drawing of the cyan bottles at exposure time 113 000 μs ; (f) local enlarged drawing of the white bottles at exposure time 53 000 μs after time domain superposition; (g) local enlarged drawing of the cyan bottles at exposure time 53 000 μs after time domain superposition.

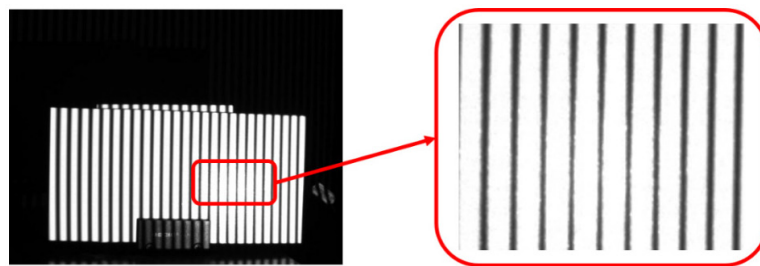


Figure 21. Phenomenon of the PSF.

reflection well. Moreover, algorithm-based techniques are also vulnerable to the specular reflection because the phase information is lost when specular reflection happens.

In this case, the method based on the polarization [19] is more suitable. Although polarizers can eliminate the influence of specular reflection, it also reduce the light intensity of the whole scene. Figure 19(a) shows that saturation is avoided by sacrificing the SNR of the cyan porcelain bottle. That leads to a very poor measurement result of the cyan bottle shown in figure 20(c). However, directly improving the projected light intensity makes the white bottle saturated shown in figure 19(c) which leads to an incorrect measurement result of the white bottle shown in figure 20(d). Our method can be used together with the polarization method to solve this problem. The measurement result is shown in figures 20(f) and (g). It can be seen that the 3D reconstructions of these two bottles are both of good quality.

5. Discussion

From the experimental results, it can be seen that the time domain superposition method is not only used to remove the influence of noise as traditional image processing technology, but also a simple and efficient method which is effective to extend the dynamic range of FPP systems. Compared with conventional HDR methods that focus on saturated region, our method has the following advantages.

- (1) Our method can find the optimal exposure time more easily. We have only to adjust the camera exposure to ensure that the region with the highest reflectivity is not saturated. Whether captured images have saturated part or not can be reflected in the image grayscale intuitively. For conventional HDR methods, the reflected light intensities of 256 and 300 (for an 8-bit camera) have the same grayscale (255) in the captured images. It is difficult for them to determine whether the given scene is in measuring range. So they usually require multiple attempts at getting the optimal exposure which makes the measurement very time-consuming.
- (2) Our method is insensitive to the camera's point spread function (PSF). In actual measurement, we find that the saturated pixels erode the neighboring dark pixels shown in figure 21. This phenomenon is believed to be the imperfect averaging produced when significant intensity variations occur within the PSF, thus introducing a bias in the detected phase. In other words, saturated pixels increase the light intensities of their adjacent pixels significantly. Sometimes the light intensities of these affected pixels are less than 255 (for an 8-bit camera). For some conventional HDR methods, these affected pixels are thought to be the optimal pixels that results in considerable errors. By contrast, images captured by our method have no saturated pixels, so PSF has little influence on our measurement results.

- (3) Our method has the characteristic of easy implementation. Compared with the other methods, our method does not need complex calculation and additional hardware. So it can be easily transplanted to the existing FPP systems. Moreover, because of its easy operation, our method does not need excessive human intervention during the measurement. Computers instead of experimenters can deal with tedious and repetitive measurement tasks that provides the potential to measure the HDR objects automatically.

6. Conclusion

In this paper, the reason why phase error occurs in the low-reflection region is analyzed in detail. Based on the Gaussian noise model, we have developed a method called time domain superposition to extend the dynamic range of FPP systems by reducing the phase error of low-reflection regions. Some experiments are given to illustrate the validation and effectiveness of the proposed method. As the proposed method is a mathematical solution, it can be applied to the existing FPP systems without any raise of hardware costs. Further, it can also be used together with other HDR methods based on FPP to get better measurement results.

Acknowledgment

This work was supported by the National Natural Science Fund of China (61722506, 61705105, 111574152), National Key Technologies R&D Program of China (2017YFF0106403), Final Assembly '13th Five-Year Plan' Advanced Research Project of China (30102070102), The Key Research and Development Program of Jiangsu Province, China (BE2017162), Outstanding Youth Foundation of Jiangsu Province of China (BK20170034), National Defense Science and Technology Foundation of China (0106173), 'Six Talent Peaks' project of Jiangsu Province, China (2015-DZXX-009), '333 Engineering' Research Project of Jiangsu Province, China (BRA2016407), Fundamental Research Funds for the Central Universities (30917011204, 30916011322), Open Research Fund in 2017 of Jiangsu Key Laboratory of Spectral Imaging & Intelligent Sense (3091601410414), China Postdoctoral Science Foundation (2017M621747), Jiangsu Planned Projects for Postdoctoral Research Funds (1701038A), Fundamental Research Funds for the Central Universities, the Open Research Fund in 2018 of Jiangsu Key Laboratory of Spectral Imaging & Intelligent Sense (3091801410403), Fundamental Research Funds for the Central Universities (30918014115-005).

ORCID iDs

Shijie Feng  <https://orcid.org/0000-0001-8261-5276>

References

- [1] Chen F and Brown G M 2000 Overview of 3d shape measurement using optical methods *Opt. Eng.* **39** 10–22
- [2] Blais F 2004 Review of 20 years of range sensor development *Proc. SPIE* **13** 228–40
- [3] Feng S, Zuo C, Tao T, Hu Y, Zhang M, Chen Q and Gu G 2018 Robust dynamic 3d measurements with motion-compensated phase-shifting profilometry *Opt. Lasers Eng.* **103** 127–38
- [4] Feng S, Zhang L, Zuo C, Tao T, Chen Q and Gu G High dynamic range 3d measurements with fringe projection profilometry: a review *Meas. Sci. Technol.* **29** 122001
- [5] Zhang S and Yau S T 2009 High dynamic range scanning technique *Opt. Eng.* **48** 033604
- [6] Waddington C and Kofman J 2010 Saturation avoidance by adaptive fringe projection in phase-shifting 3d surface-shape measurement *Int. Symp. on Optomechatronic Technologies* (IEEE) pp 1–4
- [7] Lin H, Gao J, Mei Q, He Y, Liu J and Wang X 2016 Adaptive digital fringe projection technique for high dynamic range three-dimensional shape measurement *Opt. Express* **24** 7703
- [8] Hu E, He Y and Wu W 2010 Further study of the phase-recovering algorithm for saturated fringe patterns with a larger saturation coefficient in the projection grating phase-shifting profilometry *Opt. Int. J. Light Electron Opt.* **121** 1290–4
- [9] Jiang C, Bell T and Zhang S 2016 High dynamic range real-time 3d shape measurement *Opt. Express* **24** 7337–46
- [10] Chen B and Zhang S 2016 High-quality 3d shape measurement using saturated fringe patterns *Opt. Lasers Eng.* **87** 83–9
- [11] Srinivasan V, Liu H-C and Halioua M 1984 Automated phase-measuring profilometry of 3d diffuse objects *Appl. Opt.* **23** 3105–8
- [12] Rathjen C 1995 Statistical properties of phase-shift algorithms *J. Opt. Soc. Am. A* **12** 1997–2008
- [13] Li J, Hassebrook L G and Guan C 2003 Optimized two-frequency phase-measuring-profilometry light-sensor temporal-noise sensitivity *JOSA A* **20** 106–15
- [14] Kamgar-Parsi B R and Kamgar-Parsi B Z 1989 Evaluation of quantization error in computer vision *IEEE Trans. Pattern Anal. Mach. Intell.* **11** 929–40
- [15] Gonzalez R C 2016 *Digital Image Processing* (New York: Pearson)
- [16] Sathaki T 2011 *Image Fusion: Algorithms and Applications* (Amsterdam: Elsevier)
- [17] Zuo C, Huang L, Zhang M, Chen Q and Asundi A 2016 Temporal phase unwrapping algorithms for fringe projection profilometry: a comparative review *Opt. Lasers Eng.* **85** 84–103
- [18] Liu K 2010 Real-Time 3d Reconstruction by Means of Structured Light Illumination *PhD Thesis* University of Kentucky
- [19] Chen T, Lensch H P, Fuchs C and Seidel H-P 2007 Polarization and phase-shifting for 3d scanning of translucent objects *IEEE Conf. on Computer Vision and Pattern Recognition* (IEEE) pp 1–8